Rare Metal Materials and Engineering
Volume 55, Issue 8, August 2026
Available online at www.rmme.ac.cn

Science Press

Cite this article as: Gan Yisheng, Wang Haiyang, Zhong Hong, et al. Effect of Withdrawal Rate on Microstructure and Creep Performance of Directionally Solidified Mar-M247LC Superalloy[J]. Rare Metal Materials and Engineering, 2026, 55(08): 1865-1875. DOI: https://doi.org/10.12442/j.issn.1002-185X.20250488.

ARTICLE

Effect of Withdrawal Rate on Microstructure and Creep Performance of Directionally Solidified Mar-M247LC Superalloy

Gan Yisheng[1], Wang Haiyang[2,3], Zhong Hong[1], Zhu Jiaxi[1], Li Bo[1], Feng Zhenyu[1], Li Shuangming[1]

[1] State Key Laboratory of Solidification Processing, Northwestern Polytechnical University, Xi'an 710072, China; [2] State Key Laboratory of Clean and Efficient Turbomachinery Power Equipment, Deyang 618000, China; [3] Dongfang Electric Corporation Dongfang Turbine Co., Ltd, Deyang 618000, China

Abstract: The effect of withdrawal rate on microstructure and creep performance of directionally solidified (DS) Mar-M247LC superalloy was investigated. Results show that an increase in withdrawal rate of DS specimens leads to a reduction in primary dendrite arm spacing (from 479 μm to 322 μm), and the average size of γ' precipitate decreases from 460 nm to 345 nm in interdendritic region and from 298 nm to 203 nm in dendritic core. In addition, the carbide morphology changes from blocky to script-like. The heat treatment leads to the formation of distinct cuboidal γ' precipitates. And the volume fraction of γ' precipitates in heat-treated microstructure has a significant increase compared to that in DS microstructure. The DS superalloy under the withdrawal rate of 40 μm/s exhibits elongated raft-like γ' structure with narrowed matrix channels and regular dislocation networks, synergistically prolonging creep rupture life to 96.6 h. Fractographic analysis confirms that the superalloy exhibits a transgranular ductile fracture mode, with cracks initiating at decomposed *M*C carbides.

Key words: DS nickel-based superalloy; withdrawal rate; microstructure; creep rupture life

1 Introduction

Nickel-based superalloys are widely employed in hot-section components of gas turbines and aero-engines due to their excellent high-temperature strength and microstructural stability. To achieve superior high-temperature mechanical properties, nickel-based superalloys typically exhibit a high degree of alloying. Elements such as Cr, W, Mo, Hf, Ta, Al, and Ti are added to promote multiple strengthening mechanisms, including solid-solution strengthening and precipitation strengthening. Among these elements, the addition of Ta, Ti, and Al is particularly crucial, as it significantly promotes the precipitation of the γ' phase. This coherent nanoscale precipitate provides exceptionally effective strengthening in superalloys[1–5]. The volume fraction and size of the γ' phase significantly influence the endurance properties of the superalloys. Reducing the γ' phase size and increasing its volume fraction, which decrease the inter-particle spacing, both markedly enhance the creep resistance of superalloys[6–7]. Mar-M247 is a precipitation-strengthened Ni-Al-Cr-Co-Ta-W-Hf superalloy. Its relatively high Cr and W contents provide solid solution strengthening effect[8], while the combined addition of Ta, Ti, and Al (up to 9.5wt%) ensures a high γ' phase volume fraction, conferring outstanding creep resistance to this superalloy.

At elevated temperatures, the primary manifestation of creep damage in nickel-based superalloys occurs in the form of voids and cavitation nucleation at grain boundaries[3]. Grain boundaries perpendicular to the stress direction often act as crack initiation sites or propagation paths. Directional solidification (DS) technique promotes the growth of columnar grains, which effectively eliminates transverse grain boundaries that are harmful to creep resistance, thereby significantly enhancing the creep life of superalloys[9–10].

Received date: September 23, 2025
Foundation item: Supported by State Key Laboratory of Clean and Efficient Turbomachinery Power Equipment (DEC8300CG202320387EE280522)
Corresponding author: Wang Haiyang, Ph. D., State Key Laboratory of Clean and Efficient Turbomachinery Power Equipment, Deyang 618000, P. R. China, E-mail: fachcy@163.com; Zhong Hong, Ph. D., Associate Professor, State Key Laboratory of Solidification Processing, Northwestern Polytechnical University, Xi'an 710072, P. R. China, E-mail: zhonghong123@nwpu.edu.cn

However, the high concentration of solute elements can lead to segregation during DS process. Elements with a solidification partition coefficient k<1, such as Nb, Ta, Ti, and Hf, preferentially segregate at the interdendritic regions, causing chemical inhomogeneity[11–12]. Severe segregation promotes the formation of substantial amounts of γ/γ' eutectic in the interdendritic regions. The presence of γ/γ' eutectic reduces the tensile properties and creep strength of superalloys. Its coarse structure readily acts as a stress concentration point during creep, inducing crack initiation.

Furthermore, in the Mar-M247LC superalloy, elements such as Ta, W, and Hf promote the formation of *M*C carbides. These primary *M*C carbides are unstable at high temperatures and prone to degenerative decomposition reactions[13–14]. Qin et al[15] investigated the influence of primary *M*C decomposition on the microstructure and endurance properties of nickel-based superalloys. Results show that the decomposition involves interdiffusion of elements between the primary *M*C carbides and the γ matrix, which can increase the volume fraction of γ' phase to some extent, thereby improving the endurance properties of superalloy. Zhang et al[13] conducted long-term thermal exposure experiments on DS nickel-based superalloys. Results show that primary *M*C carbides decompose at grain boundaries, promoting the formation of $M_{23}C_6$ and M_6C carbides. Granular $M_{23}C_6$ carbides can pin dislocations and inhibit grain boundary sliding during deformation[16]. However, when carbides form a continuous chain-like structure along grain boundaries, they promote grain-boundary coarsening, making the boundaries more susceptible to becoming crack initiation sites. Based on Mar-M247 superalloy, Mar-M247LC superalloy changes its carbon content to 0.07wt% , specifically to mitigate the detrimental effects of carbides on creep properties. However, elemental segregation inherent to DS process still leads to the formation of coarse interdendritic *M*C carbides[8,17].

Subsequent solution heat treatment processes aim to activate elemental diffusion at high temperatures to promote the dissolution of the eutectic γ' phase and carbides. However, given the low melting point of the eutectic phase, the solution temperature cannot be too high to avoid incipient melting. Under these constraints, the dissolution of some eutectic improves the saturation level of the matrix. Consequently, this highly saturated matrix cannot further dissolve eutectic, resulting in residual eutectic retained in the superalloy[2,18–20]. Therefore, interdendritic segregation and similar inhomogeneities cannot be completely eliminated, and they will still affect the properties of the superalloy to some extent. Furthermore, merely extending the duration of the solution heat treatment not only reduces production efficiency but also yields only limited improvement in solute diffusion. Crucially, prolonging the duration of heat treatment can lead to the formation of pores/cavities within the superalloy, ultimately degrading its creep life[16,21–23]. Consequently, compared with relying solely on heat treatment, directly controlling the solidification parameters to regulate the initial segregation profile of the superalloy is more effective in enhancing its microstructural homogeneity.

In DS process, both the temperature gradient (G) and the withdrawal rate (V) are key parameters influencing the microstructure. However, since adjusting the temperature gradient often relies on equipment and is relatively unstable, controlling the withdrawal rate offers a more direct and efficient approach to adjusting the solidification microstructure of superalloys, showing significant importance for optimizing their mechanical properties[9,24]. Previous studies have demonstrated that increasing the withdrawal rate refines the microstructure. For instance, Li et al[25] investigated the solidification characteristics and high-temperature tensile properties of IN713C superalloy at different withdrawal rates using DS. They demonstrated that increasing the withdrawal rate promotes the micro-segregation of Mo, Nb, and Zr, favoring the precipitation of γ/γ' eutectic and borides. An appropriate increase in withdrawal rate is beneficial to improving high-temperature tensile properties. However, when the withdrawal rate exceeds 50 μm/s, the increased γ/γ' eutectic and borides lead to a decrease in high-temperature strength. Liu et al[26] studied the effect of withdrawal rate on the segregation behavior of the Ru- and Re-containing nickel-based single-crystal superalloys. They revealed that as the withdrawal rate increases, the segregation degree of Al, Ta, W, and Re initially increases and then decreases. The reduction in segregation at fast withdrawal rates is attributed to the refinement of the dendritic structure. Furthermore, the addition of Ru and Re increases the segregation degree of Al and Ta.

Therefore, this study investigated the influence of withdrawal rate (V=20–70 μm/s) on the as-cast microstructure of DS Mar-M247LC and its subsequent creep performance at 980 ℃/220 MPa. Additionally, the mechanisms governing creep fracture under these specific conditions were investigated. The primary focus was to elucidate how withdrawal rate governs critical microstructural characteristics, including primary dendrite arm spacing (PDAS), γ' precipitate size/morphology/volume fraction, and carbide formation. Ultimately, the creep rupture life of the superalloy was obtained. This research aimed to identify the optimal withdrawal rate, which can optimize microstructural characteristics, such as refined γ', narrowed matrix channels, and regular dislocation networks, thus enhancing creep resistance.

2 Experiment

The master alloy ingot of nickel-based Mar-M247LC superalloy was used as the raw material, and the nominal composition is listed in Table 1. DS superalloy rods were fabricated via liquid metal cooling installation under argon atmosphere at withdrawal rates of 20, 40, and 70 μm/s, which were named as WR20, WR40, and WR70 in this research, respectively. Subsequently, the DS rods were subjected to solution and aging heat treatments. The solution treatment is 1228 ℃/2 h+1240 ℃/2 h+1255 ℃/2 h/air cooling (AC). The aging treatment is 1079 ℃/4 h/AC+870 ℃/20 h/AC. All heat treatments were performed with the rods vacuum-sealed in

Table 1 Nominal chemical composition of Mar-M247LC superalloy (wt%)

Al	Cr	Co	Ta	W	Hf	Ti	Mo	Zr	C	B	Ni
5.500	8.000	9.500	3.300	9.400	1.400	0.700	0.500	0.020	0.070	0.016	Bal.

quartz ampoules.

Creep rupture tests were conducted on heat-treated Mar-M247LC superalloys with different withdrawal rates under the conditions of 980 ℃/220 MPa using an RDL30 creep testing machine. The heat-treated rods were machined into tensile creep specimens with a gauge length of 25 mm and a gauge diameter of 5 mm.

During the test, real-time monitoring of specimen temperature was achieved using thermocouples attached at three locations along the gauge length. For each condition, creep tests were performed using two independent specimens. All tests were repeated, and the obtained results are reproducible.

Metallographic specimens were sectioned from the DS specimen and heat-treated specimen. All metallographic specimens were mechanically ground using abrasive paper of 400#–3000# and polished using diamond paste of 1.5 μm. Then, all metallographic specimens were electrolytically etched in a solution of 45vol% H_2SO_4+42vol% HNO_3+13vol% H_3PO_4 at 5 V for 3–5 s to expose the γ' precipitates, and they were chemically etched with a solution of 10 mL HNO_3+20 mL HF+30 mL glycerol to expose the γ channel.

Dendritic structures were observed using an Olympus OLS400 laser scanning confocal microscope. General microstructural characterization was performed using a scanning electron microscope (SEM, Zeiss Gemini500). Quantitative microstructural analysis was conducted using the image analysis software Image-Pro Plus 6.0. The area fraction of the γ' phase was measured by image thresholding according to the grey values. To ensure statistical significance, at least three representative images were analyzed for each condition.

Specimens for electron backscattered diffraction (EBSD) analysis were electropolished in a solution of 10vol% perchloric acid in ethanol at 20 V for 20 s. The phase statistics of the superalloy were analyzed on a TESCAN AMBER SEM operated at an accelerating voltage of 20 kV, a probe current of 10 nA, and a scan step size of 0.05 μm.

Dislocation configurations were observed on the transmission electron microscope (TEM, FEI Talos F200X) operated at 200 kV. Thin foils for TEM were prepared by punching them into 3 mm-thick disks, mechanical grinding until the thickness is approximately 40 μm, and twin-jet electropolishing in a solution of 10vol% perchloric acid in ethanol at −30 ℃ and 30 V.

3 Results and Discussion

3.1 Microstructural evolution in DS Mar-M247LC superalloy

3.1.1 Microstructure characteristic

The microstructure of DS Mar-M247LC superalloy undergoes significant evolution with the increase in withdrawal rate, as shown in Fig. 1. Microstructure analysis (Fig. 1a–1c) reveals progressive refinement of the dendritic structure with the increase in withdrawal rate. This dendrite refinement can be quantified by a decrease in PDAS from 479±22 μm (WR20) to 403±27 μm (WR40) and 322±20 μm (WR70) (Fig. 1j), which is primarily governed by the increased thermal undercooling and the reduced local solidification time at higher withdrawal rates, restricting dendritic coarsening.

Concurrently, solute segregation dominates the formation of interdendritic phase. Because the partition coefficient $k<1$, γ'-forming elements (Ti, Ta, and Al) are rejected into the interdendritic liquid during solidification. This progressively enriches the solutes in the remaining liquid phase, thus promoting the formation of a substantial interdendritic eutectic.

Phase transformation is further evidenced in γ' precipitates (Fig. 1d – 1i). γ' precipitate in both dendritic core and interdendritic region of WR20 exhibits the maximum size and a butterfly morphology. With the increase in withdrawal rate, γ' precipitate undergoes progressive refinement and transitions toward a cuboidal shape. Notably, the size of γ' precipitates in dendritic cores is consistently smaller than that in interdendritic regions. Quantitative analysis (Fig. 1k – 1l) confirms that the higher withdrawal rates reduce the average diameter of γ' while increasing its volume fraction in both regions.

According to the scaling law by Kurz et al[27], PDAS (λ_1) changes with temperature gradient (G) and cooling rate (R), as follows:

$$\lambda_1 \propto G^{-0.5} R^{-0.25} \quad (1)$$

In DS process with constant G (characteristic of the experimental system), PDAS is dominantly controlled by R. Since cooling rate R correlates linearly with withdrawal rate V ($R=GV$), Eq. (1) can be simplified to $\lambda_1 \propto G^{-0.75} V^{-0.25}$. Experimental data (Fig. 1j) confirm this inverse relationship, showing progressive PDAS reduction from 479±22 μm (WR20 specimen) to 322±20 μm (WR70 specimen) with the increase in V.

Carbides in the superalloy are consistently localized within interdendritic regions across all withdrawal rates, as evidenced in Fig.2a–2c. With the increase in withdrawal rate, the carbide morphology is transformed markedly from coarse, blocky particles to fine, script-like ones with a more dispersed distribution. Conversely, quantitative analysis in Fig. 2d reveals that the withdrawal rate exerts a negligible influence on overall carbide content. Fig.2e and 2f illustrate the energy-dispersive X-ray spectroscope (EDS) point-analysis results for blocky and rod-like carbides, respectively. The results indicate that Ta is the primary element in these carbides, and Hf and W can also be detected, thereby confirming them as *M*C-type

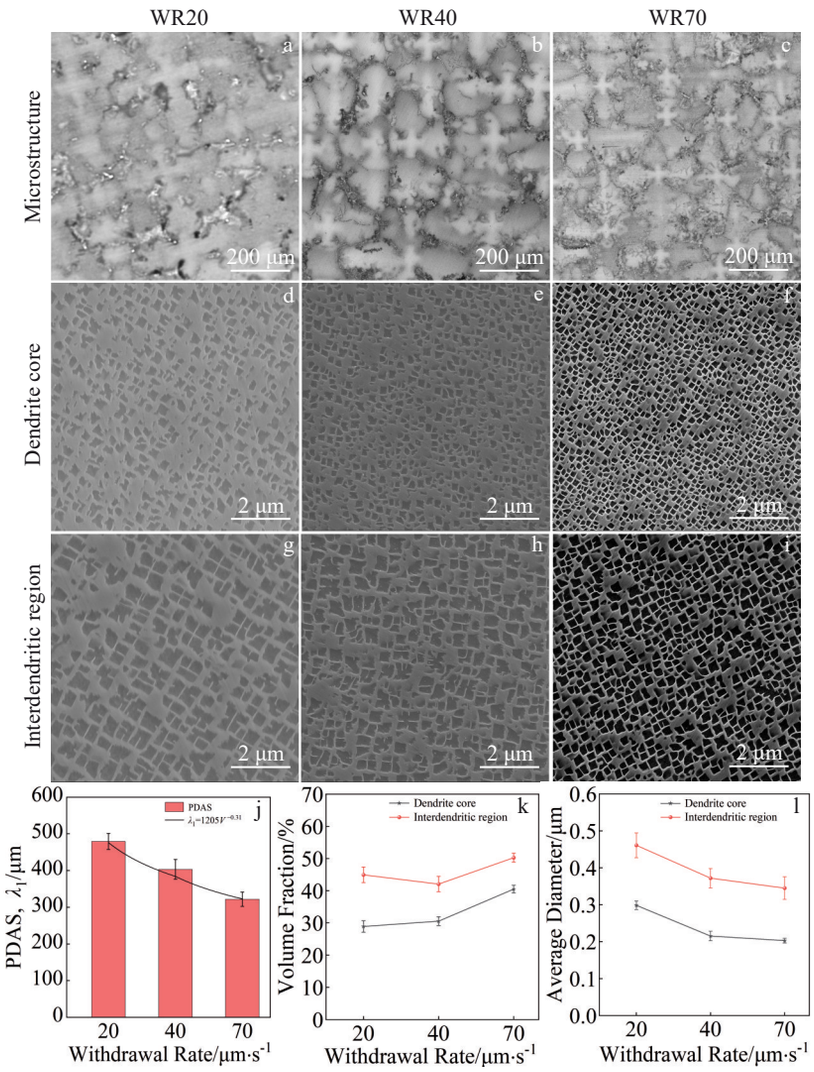

Fig.1 Microstructural evolution (a–i) and statistical analysis results (j–l) of DS Mar-M247LC superalloy with different withdrawal rates: (a–c) dendritic morphologies, (d–f) γ' phase morphologies in dendrite core, (g–i) γ' phase morphologies in interdendritic region, (j) PDAS, (k) volume fraction of γ' phase, and (l) average diameter of γ' phase

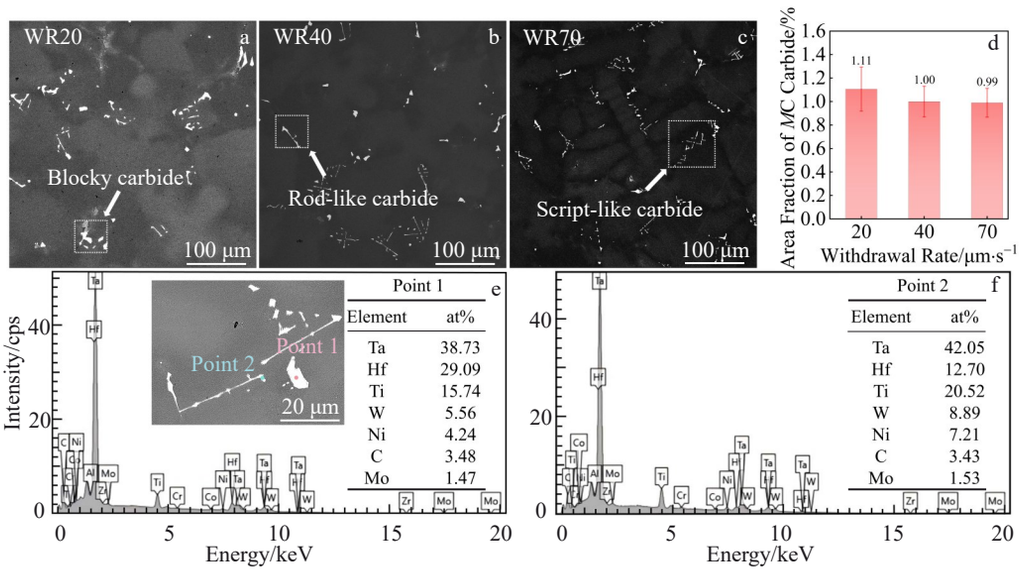

Fig.2 Carbide distribution characteristics with varying withdrawal rates: (a–c) SEM images; (d) area fraction of *M*C carbide; (e) EDS analysis results of point 1; (f) EDS analysis results of point 2

carbides. Additionally, compared to the rod-like carbides, the blocky carbides have a lower Ta content and a significantly higher Hf content.

Although C is added at low levels as an interstitial solute, its pronounced segregation tendency—driven by a low solidification partition coefficient of approximately 0.21—exceeds that of other alloying elements. This preferential segregation promotes *M*C carbide formation in interdendritic regions during solidification. At faster withdrawal rates, the denser dendritic arrangements restrict carbide growth space, while an accelerated cooling rate suppresses carbide coarsening during subsequent solid-state cooling. These combined effects explain the refined carbide distribution observed at WR70 specimen, showing a characteristic of fine and script-like morphology with a more dispersed distribution[28].

3.1.2 Carbide evolution and γ' coarsening in heat-treated state

Representative SEM images in Fig. 3 and Fig. 4 illustrate the microstructural changes after heat treatment. Compared to the DS specimens, carbides in the heat-treated specimens (Fig. 3a–3c) exhibit significant refinement and more uniform distribution. Notably, the rod-like and script-like carbides decompose into small blocks or fine granular particles. Quantitative analysis reveals a substantial decrease in carbide content (from 0.99% to 0.67%) in the WR70 specimen. However, no significant variation in carbide content is observed in the WR20 (from 1.11% to 1.24%) and WR40 specimens (from 1.00% to 0.88%). Fig. 3d illustrates EDS point analysis of the primary carbides and the granular carbides that precipitate after heat treatment. The results indicate that Hf becomes the dominant element in both types of carbides. Notably, the primary carbides of heat-treated specimen show a significant increase in Hf content, along with a decrease in Ta and Ti contents compared to those of DS specimen. This change in composition suggests that the TaC and TiC components in the primary carbides are dissolved during heat treatment, allowing Ta and Ti atoms to diffuse into the γ matrix and resulting in the enrichment of Hf.

The preferred formation order of *M*C carbides, based on stability, is HfC, TaC, NbC, and TiC. Blocky *M*C carbides, which are enriched with Hf compared to the rod-like and script-like ones, demonstrate superior thermal stability. This is due to the higher resistance of HfC to decomposition compared with that of TaC at elevated temperatures[29]. In contrast to other superalloys that contain a significant amount of blocky carbides, the WR70 specimen mainly features rod-like and script-like carbides. During the heat treatment, these rod-like and script-like carbides undergo significant decomposition, whereas the blocky carbides experience far less decomposition.

*M*C carbides decompose at elevated temperatures, releasing elements (C, Ti, Ta, W, Mo) into the matrix. Crucially, the decomposition of Ta-rich script-like *M*C carbides elevates the overall Ta content of superalloy. This elevated Ta content thermodynamically stabilizes the γ' phase, increasing its equilibrium volume fraction and coarsening rate[29–30].

The observed carbide evolution directly influences the development of γ' phase. Higher-magnification views

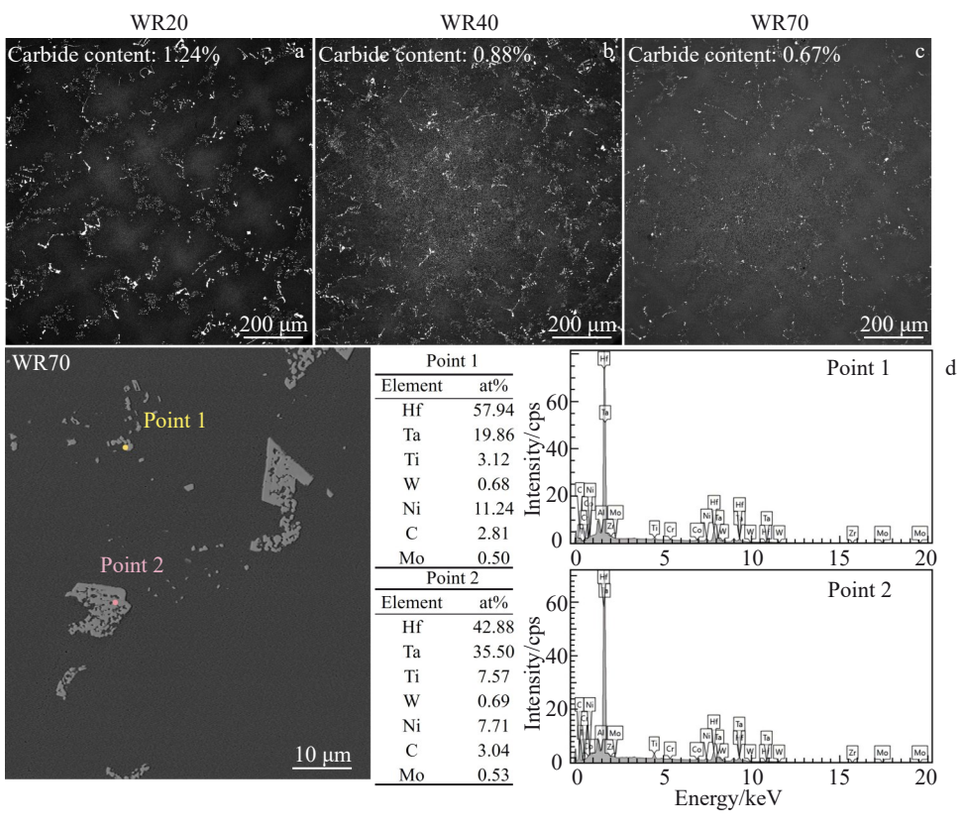

Fig.3 Morphology evolution (a–c) and EDS point analysis results (d) of carbide in different Mar-M247LC specimens after heat treatment

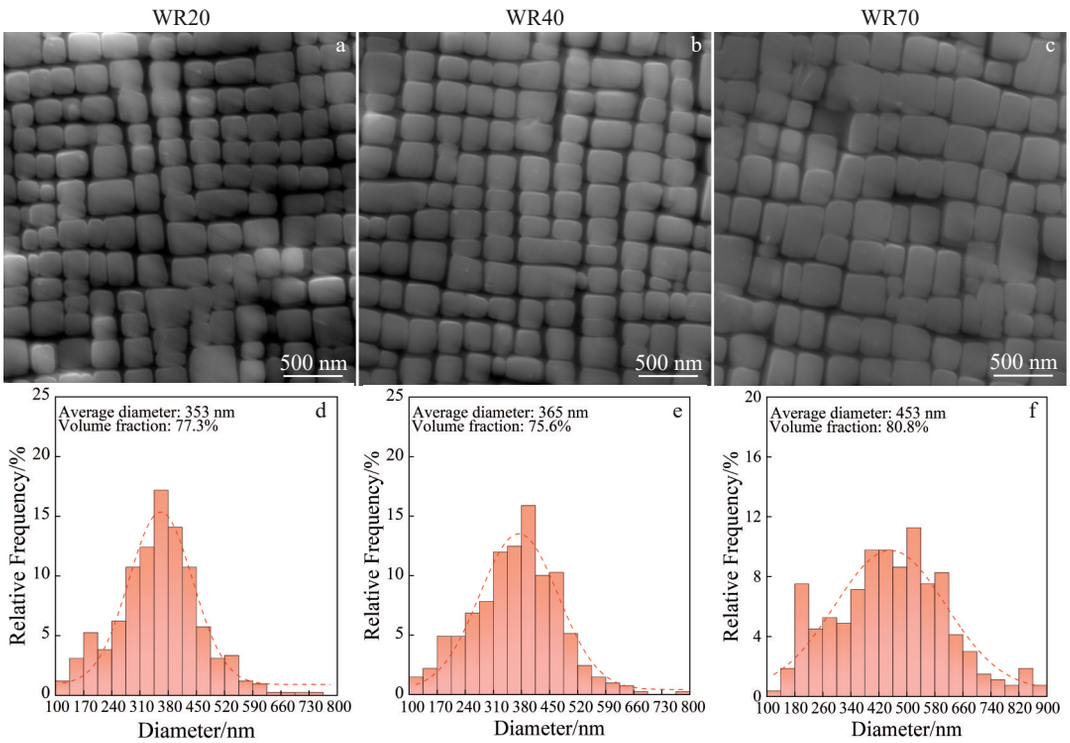

Fig.4 Microstructures (a–c) and statistical results of diameter distribution and volume fraction (d–f) of γ' precipitates in different Mar-M247LC specimens after heat treatment: (a, d) WR20; (b, e) WR40; (c, f) WR70

(Fig. 4a – 4c) confirm that the γ' phase exhibits a uniform distribution and regular cuboidal morphology across all specimens after heat treatment. Critically, the extent of *M*C carbide decomposition, i.e., Ta release, is significantly greater in the WR70 specimen than in others. Consequently, this superalloy exhibits the most pronounced increase in both the volume fraction and size of γ' phase with the increase in withdrawal rate, as quantified in Fig.4d–4f.

3.2 Withdrawal rate-dependent creep behavior

Fig. 5 presents the creep rupture curves of different specimens under the conditions of 980 ℃/220 MPa. The specimens solidified at 20, 40, and 70 μm/s exhibit rupture lives of 77.4, 96.6, and 61.3 h, respectively. With the increase in withdrawal rate, the creep rupture life of the specimens firstly increases and then decreases, indicating that the creep rupture performance exhibits an optimal value with respect to the withdrawal rate.

To investigate the underlying mechanisms of creep behavior, a meticulous examination of the fractured specimens was conducted. The morphologies of the γ' phase near the fracture surface are illustrated in Fig. 6a – 6c. All superalloys develop N-type raft-like structures perpendicular to the stress axis. In addition, the post-creep γ' morphology adjacent to fracture surfaces shows withdrawal rate-dependent characteristics. Compared to the other two specimens, WR40 specimen exhibits narrower and more elongated γ matrix channels (557 nm in width). In contrast, the γ matrix channels in the WR70 specimen show significant coarsening phenomenon (676 nm in width).

During creep deformation, the γ' phase coalesces under the

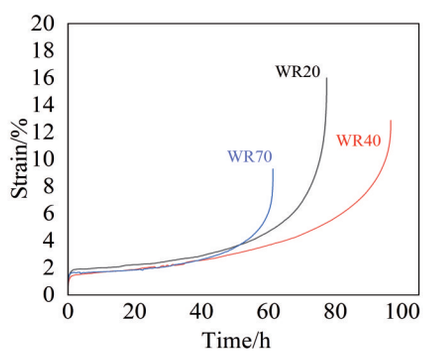

Fig.5 Creep rupture curves of different Mar-M247LC specimens at 980 ℃/220 MPa

applied stress, forming an elongated raft-like structure[30]. Under high-temperature and low-stress testing conditions, creep deformation is governed by the movement and climbing of dislocations within the γ matrix for superalloys strengthened by the γ' phase with high volume fraction. The formation of raft-like structures significantly increases the distance that the dislocations must climb, thereby enhancing the creep resistance[31–32]. Smaller γ' precipitates result in narrower γ matrix channels after the formation of raft-like structures. These narrower channels hinder dislocation movement within the γ matrix channels. Furthermore, the constricted γ matrix channels make it considerably more difficult for dislocations to bypass the γ' precipitates via climbing; instead, they are forced to shear through the γ' phase[33–36]. Consequently, the WR40 specimen, characterized by the longest rafts and the narrowest γ matrix channels,

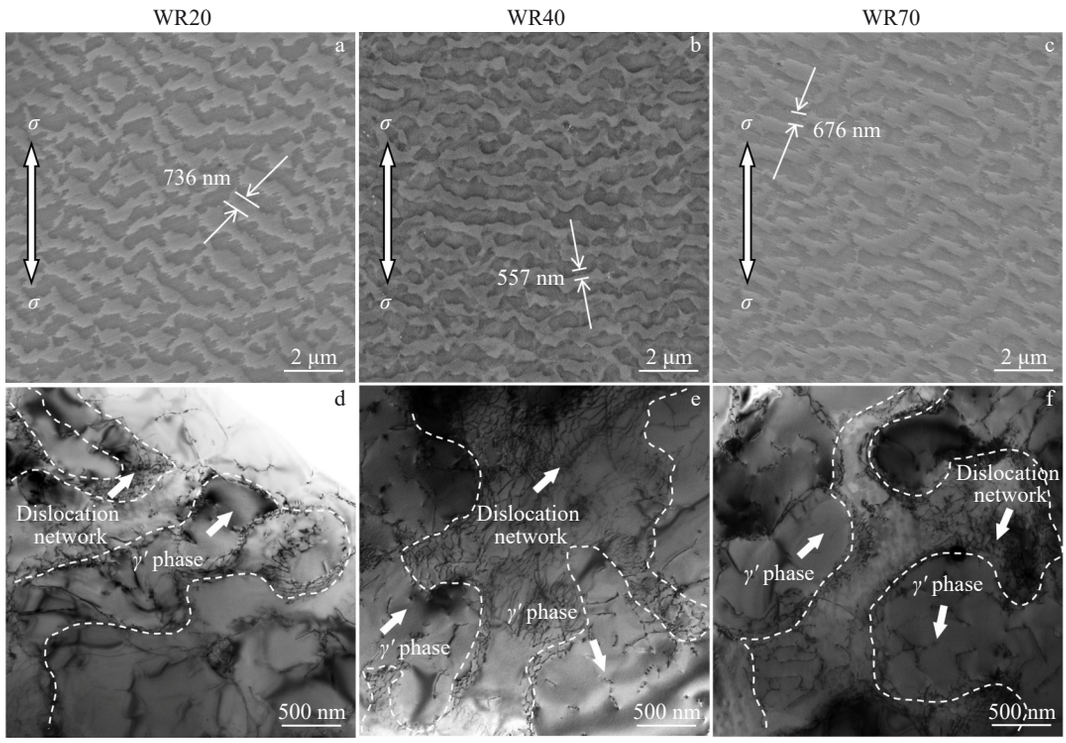

Fig.6 TEM images of γ' phase morphology near fracture surface (a–c) and dislocation networks at γ/γ' interfaces (d–f) of different Mar-M247LC specimens after creep deformation: (a, d) WR20; (b, e) WR40; (c, f) WR70

exhibits superior resistance to dislocation motion compared to the specimens solidified at other withdrawal rates. This results in the longest creep rupture life. Conversely, the deviation in the orientation of the raft-like structures in WR20 and WR70 specimens reduces their effectiveness in impeding dislocation movement, leading to shorter creep lives compared to the WR40 specimen.

Dislocation configurations under identical conditions further demonstrate microstructural divergences (Fig. 6d – 6f). It shows irregular interfacial networks with high-density dislocations penetrating the γ' phase in WR20 and WR70 specimens but larger and geometrically regular networks in WR40 specimen. The dislocations are generated within the γ matrix during the initial stage of creep. They can move through the γ matrix channels and subsequently pile up at the γ/γ' interfaces, forming dislocation networks. This accumulation leads to dislocations of high density at these interfaces. The formation of a dense dislocation network at the γ/γ' interfaces hinders the movement of subsequent dislocations within the γ matrix and impedes their shearing into the γ' phase, thereby mitigating creep damage in the superalloy. A regular dislocation network possesses higher stability, which can more effectively hinder dislocation motion and enhance the creep resistance of superalloys[37–39]. Consequently, it effectively hinders subsequent dislocation motion, resulting in superior creep rupture performance.

In addition, it should be noted that the dislocation network in the WR40 specimen demonstrates enhanced density and structural regularity, directly contributing to the prolongation of creep life through effective impedance of dislocation propagation. During the creep deformation, dislocations will nucleate in the γ matrix and propagate through γ channels, finally accumulating at γ/γ' interfaces to form dense networks. These interfacial arrays block matrix dislocation motion while preventing shear penetration into the γ' phase, thereby constraining creep damage. Crucially, geometrically ordered networks exhibit superior stability and barrier efficacy.

The dislocation network formation stems from dislocation interactions and lattice misfit (δ)[40], which can be calculated by Eq. (2)[33], as follows:

$$\delta=\frac{2(a_{\gamma'}-a_{\gamma})}{a_{\gamma'}+a_{\gamma}} \tag{2}$$

where the lattice parameters a_{γ} and $a_{\gamma'}$ depend critically on solute composition. The decomposition of Ta-rich *M*C carbides releases additional Ta into the surrounding matrix, leading to a localized increase in Ta concentration. This increases the value of a_{γ} and thereby increases the value of δ[41], promoting the formation of denser and more regular dislocation networks. As the withdrawal rate increases, the decomposition of the carbides becomes more pronounced. As a result, superalloys solidified at faster withdrawal rates exhibit greater local Ta enrichment, thus enhancing the creep resistance. However, it should be noted that the increase in Ta content simultaneously increases the γ' phase content in the superalloy, which also promotes coarsening of the γ' phase during creep. An excessive amount of the γ' phase can have an adverse effect on the creep properties[42]. In the WR70 specimen, γ' phase coarsening results in wider γ matrix channels. This facilitates rapid dislocation motion and climb-mediated bypass of γ' precipitates. Consequently, the

dislocation network density of the γ/γ' interface decreases, ultimately decreasing the creep resistance.

3.3 Microstructural degradation and creep rupture mechanism

TEM images of the specimens after creep rupture testing at 980 ℃/220 MPa are shown in Fig. 7, which indicates significant microstructural degradation. The high-angle annular dark-field scanning TEM (HAADF-STEM) image, along with the corresponding EDS element mapping, demonstrates that the primary *M*C carbides undergo decomposition (Fig. 7a–7b), accompanied by the precipitation of Cr-rich $M_{23}C_6$ carbides. Importantly, continuous γ' films form around these degraded primary *M*C carbides, and microcracks are predominantly localized near carbide clusters (Fig. 7c–7f). Notably, $M_{23}C_6$ carbides adjacent to microcracks exhibit significantly obvious coarsening phenomenon than those in unaffected regions.

The underlying mechanism for this microstructural degradation and its link to fracture initiation can be described as follows. During creep, the TaC component within primary *M*C carbides decomposes due to its inferior thermal stability relative to HfC, following the reaction: $MC+\gamma \rightarrow M_{23}C_6+\gamma'$ [13,29]. This process consumes solid-solution strengthening elements (e. g. Cr) in the γ matrix, thereby diminishing solid-solution strengthening effect. Additionally, the formation of continuous γ' films lowers the resistance to dislocation movement at the γ/γ' interfaces, thus weakening the strengthening effect at the interfaces. As a result, dislocations can more readily destroy the dislocation network under applied stress and cut into the γ' phase, eventually accumulating near the carbides. This leads to stress concentration around the carbides and promotes crack initiation in these regions. Furthermore, coarsening of $M_{23}C_6$ carbides during creep decreases their pinning effect on dislocations. Consequently, the regions surrounding the decomposed primary *M*C carbides become microstructural weak zones, acting as preferred sites for microcrack initiation and propagation.

The fracture morphologies of the three specimens after creep tests are presented in Fig.8a–8c. As shown in the inserts, all specimens exhibit pronounced necking and display clearly visible dimple rupture features, showing a transgranular ductile fracture mechanism under these conditions. EDS analysis of microcracks in the ruptured specimens at different withdrawal rates (Fig. 8d – 8f) reveals the enrichment of carbide-forming elements (Ta, W, and Hf) around the microcracks. This confirms that crack initiation and propagation occur preferentially near carbide particles. Therefore, the localized reduction in strength surrounding decomposed primary *M*C carbides is identified as the predominant mechanism responsible for creep fracture initiation.

The observed dislocation behavior is integrated into a schematic illustration of the overall creep fracture mechanism for Mar-M247LC at 980 ℃/220 MPa, as shown in Fig. 9. Dislocations begin to nucleate within the γ matrix channels and glide under the applied stress, gradually accumulating at the γ/γ' interfaces. This accumulation results in extensive dislocation pile-up and the formation of interfacial dislocation

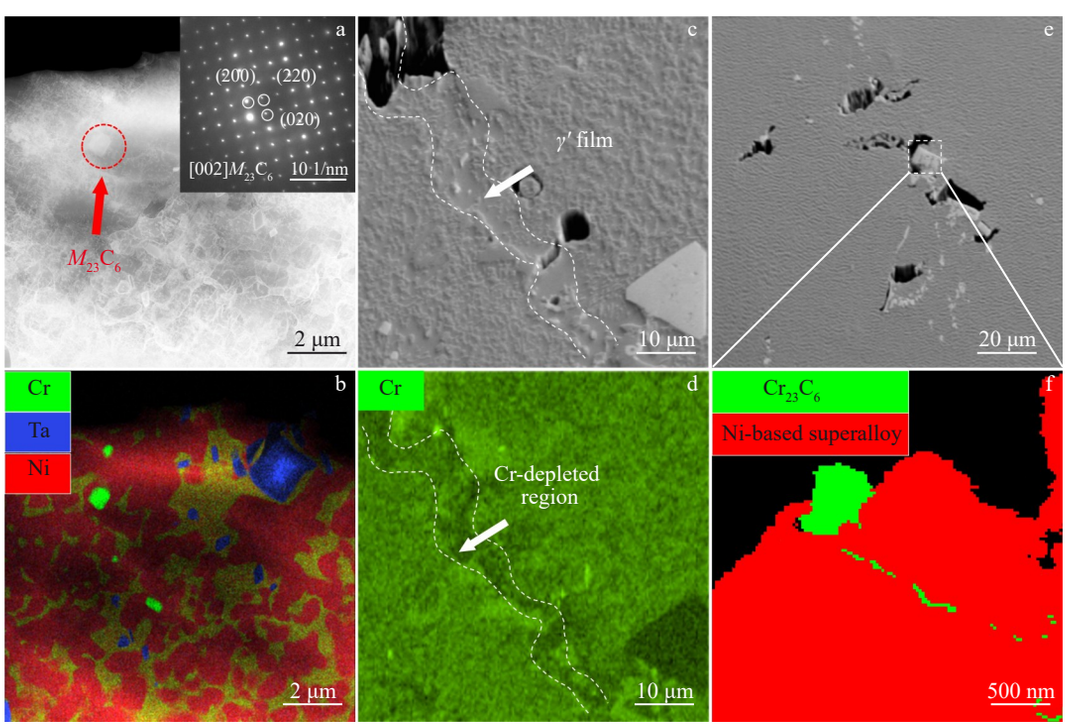

Fig.7 Microstructural characterization of creep-fractured WR20 (a–b) and WR70 (c–f) specimens: (a) HAADF-STEM image of carbides; (b) EDS element mapping corresponding to Fig. 7a; (c) SEM image of Cr-depleted region; (d) EDS element mapping corresponding to Fig. 7c; (e) SEM image of microcracks; (f) EBSD phase map highlighting $Cr_{23}C_6$ phase

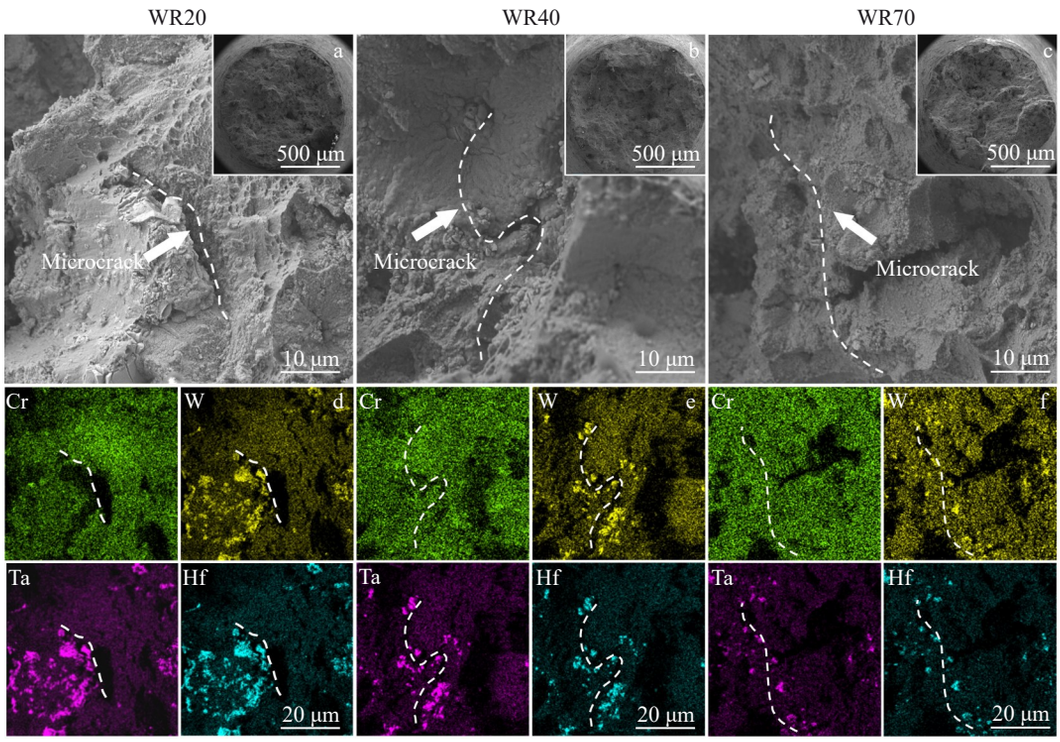

Fig.8 SEM images of the creep fracture morphologies (a – c) and corresponding EDS element mappings (d – f) of different Mar-M247LC specimens: (a, d) WR20; (b, e) WR40; (c, f) WR70

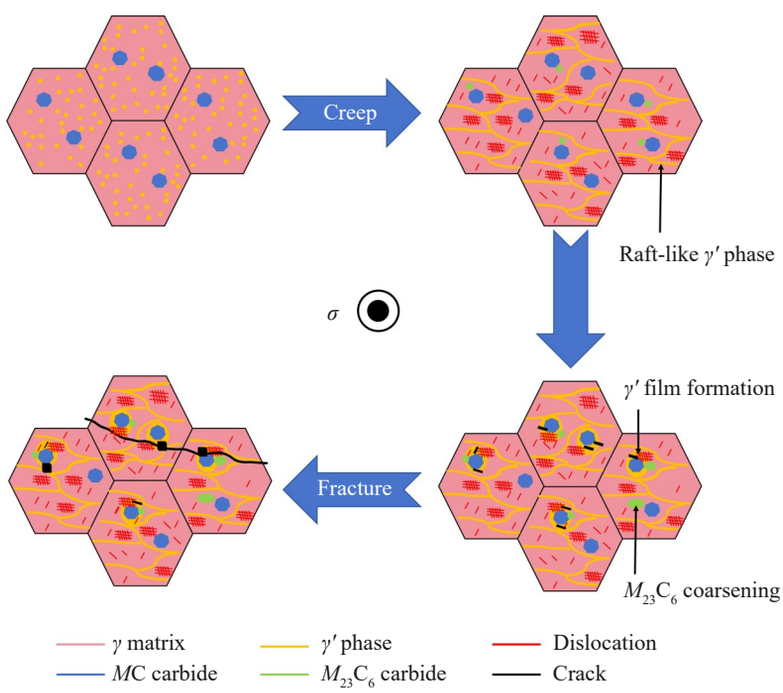

Fig. 9 Schematic diagram of the key stages in creep rupture mechanism of Mar-M247LC superalloy at 980 °C/220 MPa

networks. During the creep process, the primary carbides in the superalloy decompose, leading to the precipitation of $M_{23}C_6$ carbides and the formation of continuous γ' films. As stress increases, dislocations in the γ matrix disrupt the dislocation networks and penetrate the γ' precipitates. These dislocations pile up at the carbides and induce significant stress concentration, eventually triggering crack initiation. These cracks are initiated discontinuously within the specimen and propagate perpendicular to the applied stress axis. Ultimately, the coalescence of these microcracks results in predominantly transgranular fracture.

Although variations in the withdrawal rate can influence the

microstructure and creep performance of the Mar-M247LC superalloy, no change in the fracture mechanism is observed. All tested specimens display nearly identical fracture mechanisms. Compared to superalloys solidified at other withdrawal rates, the WR40 specimen exhibits elongated raft-like γ' structures and significantly narrower γ matrix channels. This specific microstructural configuration promotes the development of denser and more regular dislocation networks at the γ/γ' interfaces. These enhanced dislocation networks act as potent barriers, effectively impeding dislocation glide within the matrix channels. This superior dislocation confinement directly contributes to the prolonged creep rupture life observed in the WR40 specimen.

4 Conclusions

1) Increasing the withdrawal rate significantly refines the dendritic structure and transforms the morphology of *M*C carbides from coarse blocky to fine script-like. Following standard heat treatment, the fine primary carbides exhibit an enhanced propensity for decomposition into minor granular particles. This decomposition releases additional Ta into the matrix, promoting γ' precipitate coarsening, with WR70 specimen exhibiting the coarsest γ' morphology.

2) WR40 specimen exhibits the longest creep rupture life of 96.6 h under the condition of 980 ℃/220 MPa. The superior performance originates from the narrowest γ matrix channels and the densest dislocation network at the γ/γ' interfaces, which effectively impede dislocation motion. The Ta released from *M*C carbide increases the γ/γ' lattice mismatch, further facilitating the formation of this beneficial dislocation network.

3) During creep deformation, the decomposition of primary *M*C carbides depletes Cr from the surrounding γ -matrix, which weakens the solid-solution strengthening effect, and simultaneously promotes the formation of adjacent continuous γ' films. This synergistic effect critically reduces the localized strength in these regions, creating preferential sites for microcrack nucleation. Once initiated, these microcracks propagate preferentially along paths decorated with coarsened $M_{23}C_6$ carbides, ultimately leading to macroscopic transgranular fracture.

References

1 Gai Y C, Zhang R, Yang J X *et al*. *Materials Science and Engineering A*[J], 2022, 842: 143079

2 Peng P, Lu L, Liu Z J *et al. Journal of Alloys and Compounds*[J], 2022, 920: 165886

3 Reed R C. *The Superalloys: Fundamentals and Applications*[M]. Cambridge: Cambridge University Press, 2006

4 Ge M T, Wang X G, Li Y M *et al. Acta Metallurgica Sinica* (*English Letters*)[J], 2024, 37(11): 1921

5 Fei X, Sheng N C, Sun S J *et al. Acta Metallurgica Sinica* (*English Letters*)[J], 2024, 37(12): 1995

6 Peng Z C, Tian G F, Jiang J *et al. Materials Science and Engineering A*[J], 2016, 676: 441

7 Bhowal P R, Wright E F, Raymond E L. *Metallurgical Transactions A*[J], 1990, 21(6): 1709

8 Baldan R, da Rocha R L P, Tomasiello R B *et al. Journal of Materials Engineering and Performance*[J], 2013, 22(9): 2574

9 Yang Y Z, Wen Z X, Pei H Q *et al. Progress in Natural Science: Materials International*[J], 2023, 33(3): 343

10 Wang H W, Zhang X L, Meng J *et al. Journal of Alloys and Compounds*[J], 2021, 873: 159794

11 Mirak A, Fathi M. *Materials Characterization*[J], 2022, 194: 112449

12 Ai C, Zhou J, Li S S *et al. Journal of Alloys and Compounds*[J], 2016, 660: 159

13 Zhang H W, Qin X Z, Wu Y S *et al. Materials Science and Engineering A*[J], 2018, 718: 449

14 Wang J, Zhou L Z, Qin X Z *et al. Materials Science and Engineering A*[J], 2012, 553: 14

15 Qin X Z, Wang J Q, Cheng S H *et al. Materials Science and Engineering A*[J], 2023, 881: 145416

16 Bor H Y, Wei C N, Jeng R R *et al. Materials Chemistry and Physics*[J], 2008, 109(2–3): 334

17 Szczotok A, Rodak K. *IOP Conference Series: Materials Science and Engineering*[J], 2012, 35: 012006

18 Rakoczy Ł, Grudzień -Rakoczy M, Cygan R *et al. The International Journal of Advanced Manufacturing Technology* [J], 2023, 130(3–4): 1321

19 Li W Q, Zhao X B, Xu J C *et al. Vacuum*[J], 2023, 209: 111780

20 Zhao Y X, Yu J Y, Ma D X *et al. Rare Metal Materials and Engineering*[J], 2025, 54(8): 1934

21 Gao Z H, Zhang P, Li J *et al. Materials Research Letters*[J], 2023, 11(12): 1013

22 Cheng K X, Lv S W, Xuan W D *et al. Materials Characterization*[J], 2025, 224: 115009

23 Liang Z Y, Wang X G, Tan Z H *et al. Materials Characterization* [J], 2024, 215: 114137

24 Guo X T, Antonov S, Lu F *et al. Materials Science and Engineering A*[J], 2020, 770: 138530

25 Li Q L, Zhang H R, Cheng Y *et al. Journal of Alloys and Compounds*[J], 2022, 923: 166390

26 Liu G, Liu L, Ai C *et al. Journal of Alloys and Compounds*[J], 2011, 509(19): 5866

27 Kurz W, Fisher D J. *Acta Metallurgica*[J], 1981, 29(1): 11

28 Wang X J, Huang T W, Yang W C *et al. Vacuum*[J], 2021, 183: 109800

29 Li L X, Gong X F, Wang C S *et al. Acta Metallurgica Sinica* (*English Letters*)[J], 2020, 34(6): 872

30 Xia W S, Zhao X B, Yue L *et al. Journal of Alloys and Compounds*[J], 2020, 819: 152954

31 MacKay R A, Ebert L J. *Metallurgical Transactions A*[J], 1985, 16(11): 1969

32 Nathal M V, Ebert L J. *Metallurgical Transactions A*[J], 1985,

16(3): 427
33 Chen J B, Chen J Y, Wang Q J *et al. Acta Materialia*[J], 2022, 232: 117938
34 Jahangiri M R, Abedini M. *Materials & Design*[J], 2014, 64: 588
35 Cui L Q, Yu J J, Liu J L *et al. Materials Science and Engineering A*[J], 2018, 710: 309
36 Fan H, Long H B, Zhao J B *et al. Materials Science and Engineering A*[J], 2025, 921: 147603
37 Lv X Z, Zhang J X. *Journal of Alloys and Compounds*[J], 2016, 688: 449
38 Wang R, Li J R, Yue X D *et al. Rare Metal Materials and Engineering*[J], 2025, 54(10): 2445
39 Li Y X, Tian N, Zhang P *et al. Rare Metal Materials and Engineering*[J], 2025, 54(7): 1733
40 Zhang J X, Murakumo T, Koizumi Y *et al. Metallurgical and Materials Transactions A*[J], 2004, 35(6): 1911
41 Wu J J, Jiang X W, Wang Y *et al. Materials Science and Engineering A*[J], 2021, 806: 140829
42 Murakumo T, Kobayashi T, Koizumi Y *et al. Acta Materialia*[J], 2004, 52(12): 3737

抽拉速率对定向凝固Mar-M247LC高温合金微观结构及蠕变性能的影响

甘奕胜[1]，王海洋[2,3]，钟　宏[1]，朱嘉锡[1]，李　博[1]，冯振宇[1]，李双明[1]
(1. 西北工业大学 凝固技术全国重点实验室，陕西 西安 710072)
(2. 清洁高效透平动力装备全国重点实验室，四川 德阳 618000)
(3. 东方电气集团东方汽轮机有限公司，四川 德阳 618000)

摘要：研究了抽拉速率对Mar-M247LC定向凝固镍基高温合金组织和持久性能的影响。结果表明：随着定向凝固试样抽拉速率的提高，一次枝晶间距逐渐减小，从479 μm降至322 μm；γ'相平均尺寸减小（在枝晶间区域从460 nm降至345 nm，在枝晶干区域从298 nm降至203 nm）。此外，碳化物形态由块状转变为汉字状。热处理后，试样中形成了规则的立方状γ'相，且热处理后试样中的γ'相含量较定向凝固试样有显著增加。在抽拉速率为40 μm/s的条件下凝固合金会形成细长状的γ'筏形组织、狭窄的基体通道及规则的位错网络，这些因素协同作用使蠕变断裂寿命延长至96.6 h。断口分析确认该合金的断裂模式为穿晶韧性断裂，裂纹萌生于分解的*M*C碳化物处。

关键词：定向凝固镍基高温合金；抽拉速率；微观组织；蠕变寿命

作者简介：甘奕胜，男，1998年生，硕士，西北工业大学凝固技术全国重点实验室，陕西 西安 710072，E-mail：gan123@mail.nwpu.edu.cn